Self-assembly of gold nanoparticles into an adjustable plasmonic 3D lattice using Janus-type forked mesogenic ligands

Yang-yang Zhao,[a] Yu Cao,[a] Giuliano Siligardi,[b] Georg H. Mehl,*[a,c] Feng Liu,*[a] and Goran Ungar*[a,d]

[a] Yang-yang Zhao, Yu Cao, Georg H. Mehl, Feng Liu, Goran Ungar
State Key Laboratory for Mechanical Behaviour of Materials, Shaanxi International Research Center for Soft Matter, Xi'an Jiaotong University, Xi'an 710049, P. R. China
E-mail: feng.liu@xjtu.edu.cn, g.ungar@sheffield.ac.uk, g.h.mehl@hull.ac.uk
[b] Giuliano Siligardi
Diamond Light Source, Harwell, Didcot OX11 0DE, United Kingdom
[c] Georg H. Mehl
Department of Chemistry, University of Hull, Hull HU6 7RX, U.K.
[d] Goran Ungar
Department of Materials Science and Engineering, University of Sheffield, Sheffield S1 3JD, U.K.

Supporting information for this article is given via a link at the end of the document.

Abstract: We report the formation of a 3D body-centred self-assembled superlattice of gold nanoparticles whose interparticle gap, and hence its plasmonic properties, are adjustable exclusively in the *xy*-plane. Thus, even though the particles are spherical, their anisotropic packing generates tailorable plasmonic dichroism. The gold nanoparticles are coated with forked ligands containing two mesogens: either two cholesterols ("twin"), one cholesterol and one azobenzene ("Janus"), or a mixture of the two. Beside the body-centered arrangement of gold nanoparticles, the structure also contains unusual two-dimensionally modulated smectic-like layers of mesogens in an egg-box geometry. Moreover, the presence of azobenzene mesogens allows the superlattice to be melted through UV-induced photo-isomerization; the process is reversible displaying low fatigue on repeated cycling.

Introduction

Surface plasmonic resonance (SPR) properties of metal nanoparticles (NPs) offer opportunities for their use in superlenses[1], drug delivery[2], memory devices[3], field-enhanced spectroscopy[4], light harvesting photocatalysis[5, 6] and even generation of negative refractive index metamaterials[7]. For some of these applications the NPs have to be arranged in ordered arrays3 and with the anisotropic SPR. One way of controlling spatial arrangement of NPs is to coat them with mesogenic ligands. Previous work in this direction has produced a range of 2D and 3D ordered assemblies [8, 9, 10, 11, 12]. Mesogens of rod-like[13, 14, 15], disk-like[16, 17, 18] and dendritic[9, 19, 20], as well as chiral

ligands[10, 11, 21] have been employed. Furthermore, mesogenic ligands can have functions additional to those directing the assembly, such as being photoresponsive[12, 22].

Since individual plasmon oscillations on proximal particles can couple via their near-field interaction, they are sensitive to interparticle gap width [23]. This can be tuned either by adjusting the size of the ligands, by changing their grafting number, or through "dilution" of the mesogenic corona by short grafted chains bearing no mesogen ("co-ligands") [24]. For 3D lattices, ligands with divergent (e.g. dendritic) shape can be grafted on NP surface in order to efficiently fill space[9, 19]. However, divergent ligands tend to generate isotropic structures, i.e. cubic or related[9, 19, 20]. Since interparticle distance p scales as $\sim V_L^{-3}$, where V_L is ligand volume, a large change in V_L causes only a small change in p. Weak anisotropy in SPR can be achieved in such structures even if the interparticle distances in all directions are the same, provided the number of interparticle contacts is angle-dependent. Such is the case in the simple 3D hexagonal[8] and the "Bernal ice" superlattices[25] of AuNPs side-on grafted with rod-like mesogens. A more effective way of controlling the intensity and anisotropy of SPR would be to expand/contract the lattice anisotropically.

Results and Discussion

In this work we introduce forked ligands, consisting of a spacer attached to the gold NP bearing two rod-like mesogens at its outer end. Giving ligands a tapered shape helps them fill space to establish 3D structures. But to enforce anisotropy at least one of the branches must be a long rigid rod, cholesterol (**C**) in the present case. The two mesogens are either both **C**, or one of them is azobenzene (**A**). The **A** branch enables induction of an order-disorder transition through photoisomerization with UV and visible light. The particles assemble in a 3D body-centred tetragonal array, new in nanoparticles, whose interparticle distance is adjustable in 2D (*xy*-plane) thus allowing the anisotropic plasmonic effect to be tuned by changing the number of grafted forked ligands.

The chemical structure of the ligands **AC** and **CC** is shown in Figure 1. Liquid crystal (LC) properties of the forked ligands themselves are described in the supporting information (SI). Based on polarized optical microscopy (POM) and small-angle X-ray scattering (SAXS), **CC** ligand forms a chiral nematic (N*) phase, while the **AC** ligand displays a SmA* phase (Figure S2-S4, SI).

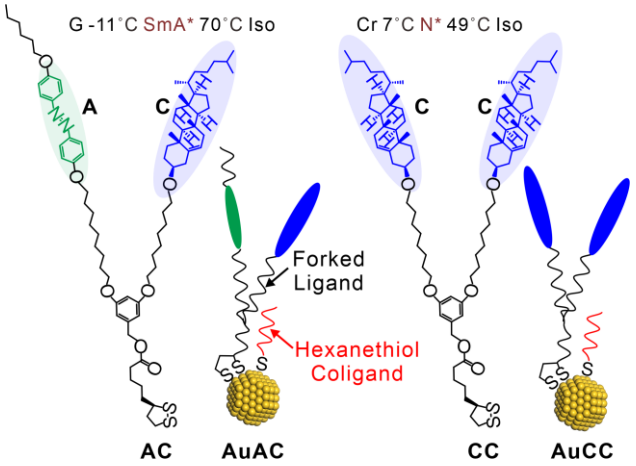

Scheme 1. The two forked ligands **AC** and **CC** and their schematic representations when attached to the AuNPs. **A** = azobenzene, **C** = cholesterol. Phases of pure non-attached ligands: G = glassy, SmA* = chiral smectic A, Iso = isotropic, Cr = crystal, N* = chiral nematic.

The LC-functionalized gold nanoparticles (**LC-AuNP**s) were coated with **AC** and **CC** ligands, with the **CC** mass fraction $\Phi_{CC} = m_{CC}/(m_{AC} + m_{CC})$ varied from 0 to 1. The resulting nanoparticles decorated with mixed ligands are denoted **AuΦ_{CC}**, while those covered with a single ligand are denoted **AuAC** and **AuCC**, respectively. First alkylthiol-covered AuNPs were synthesized by a modified Brust-Schiffrin method [26]. *n*-Hexanethiol was adopted as co-ligand since longer alkylthiols were found to inhibit interaction between mesogenic ligands[27]. Linear alkylthiol was then partially substituted by the forked ligands in a ligand exchange step. The NPs were first purified by repeated recrystallization from toluene and ethanol for more than 3 times, then by size-exclusion chromatography over Bio-Beads SX1. Preparation conditions were kept consistent for all **LC-AuNP**s. Details of the synthesis are given in SI.

High resolution 1HNMR (600M) spectroscopy was used to determine the number ratio of forked ligands to co-ligands attached to the nanoparticle surface (Figure S5). LC-AuNPs were found to be free of unbound ligands. Compared with the sharp ^{1}H-NMR peaks of the pure ligands on their own, only typically broadened signals were detected for the **LC-AuNP** systems as a result of slow rotation in solution[14,28]. The peaks at 7.84 ppm representing the aromatic protons in azobenzene, and at 5.33 ppm representing the double bond in cholesterol confirm the attachment of azobenzene and cholesterol to the gold surface. Furthermore, the peaks at 0.91 ppm representing the co-ligands. Combing all three chemical integrals, the organic molar fractions were calculated.

Samples were prepared with Φ_{CC} values of 0%, 37%, 50%, 72% and 100% (Figure S5 and Table S1). The ligand ratios of the **LC-AuNP**s were also confirmed by UV-vis spectra (Figure S6), and found to match those from NMR. All investigated AuNPs were ~2.3-2.4 nm in diameter based on transmission electron microscopy (TEM) (Figure S7).

According to TEM, thermogravimetric (TGA) (Figure S8) and NMR data, the gold content was found to be between 4-6 % by volume and 46-56 % by weight, depending on the specific composition. The ratio between mesogenic ligands and hexanethiol co-ligands ranged from 1:1 to 2:1. There were between 40 and 71 forked ligands attached to a single AuNP (Table S2), and the surface density of the ligands and co-ligands put together ranged from 5.6 to 5.9 per nm^2. These values are consistent with previous results for systems with nanoparticles of similar size decorated with different ligands[29].

The superstructure of the LC-grafted NPs was investigated by transmission SAXS and grazing-incidence SAXS (GISAXS) on Si-supported thin films. Some samples for SAXS were sheared in order to produce preferred orientation, while thin films on Si were expected to surface-align. A representative GISAXS pattern of a spin-coated sample is shown in Figure 1a, and that of transmission SAXS in Figure 1b. Patterns from other samples are in Figure S9. The two sharp diffraction peaks on the vertical (meridional) line in the GISAXS pattern of **AuCC** (Figure 1a) are in the *q* ratio 1:2. This suggests a layered structure, with the layers parallel to the (horizontal) surface. However, there are additional broad reflections on the intermediate layer lines, that are indexed as (101) and (103), the sharp meridional reflections thus becoming (002) and (004). In principle this is compatible with a centred rectangular columnar phase, plane group *c*2*mm*. However, as the diffraction is dominated by the AuNPs, a strong additional diffraction feature would be expected on the equator, caused by intracolumnar particle correlation. As this is absent, we conclude that the structure is 3-dimensionally ordered, with a body-centred tetragonal (BCT) unit cell. Consistently, only reflections with $h+k+l=2n$ are observed. The unit cell parameters for **AuCC** are a=5.97 and c=10.88 nm (Tables 1 and S3). According to the above, the NPs are arranged in layers 5.44 nm apart and shifted diagonally by $a/2$, a/2 in the *xy*-plane (see inset in Figure 3a). The transmission SAXS pattern of a sheared sample of **Au37CC** (Figure 1b) is consistent with this structure. Namely as the mesogens align parallel to the shear (Figure 7a,b) the layers orient perpendicular to it, resulting in an orientation pattern similar to that in (a).

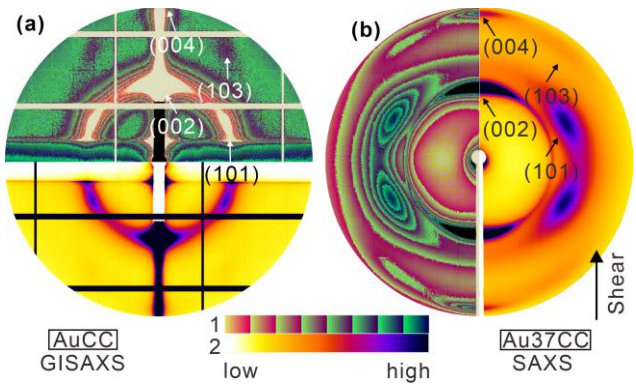

Figure 1. (a) GISAXS pattern of spin-coated **AuCC**. The top half of the fake-colour circular pattern uses colour palette 1. The bottom half of

the pattern is prepared by reflecting the top half and using colour palette 2. (b) SAXS pattern of **Au37CC** aligned by rotating a glass rod inside the sample held in a cylindrical capillary (capillary is horizontal, shear is vertical). In the left and right halves palettes 1 and 2 are used, respectively. (a,b) were recorded at room temperature.

Figure 2 shows SAXS curves of unoriented compounds from **AuAC** to **AuCC**. The position and linewidth of the four resolved peaks are consistent with those of the aligned samples. With increasing **CC** content, the broad (10*l*) peaks are seen to shift to lower *q*; between **AuAC** and **AuCC** the shift Δq is -0.41 and -0.26 nm^{-1} for (101) and (103) peaks, respectively. The observed and calculated *d*-spacings are listed in Tables S3-S7.

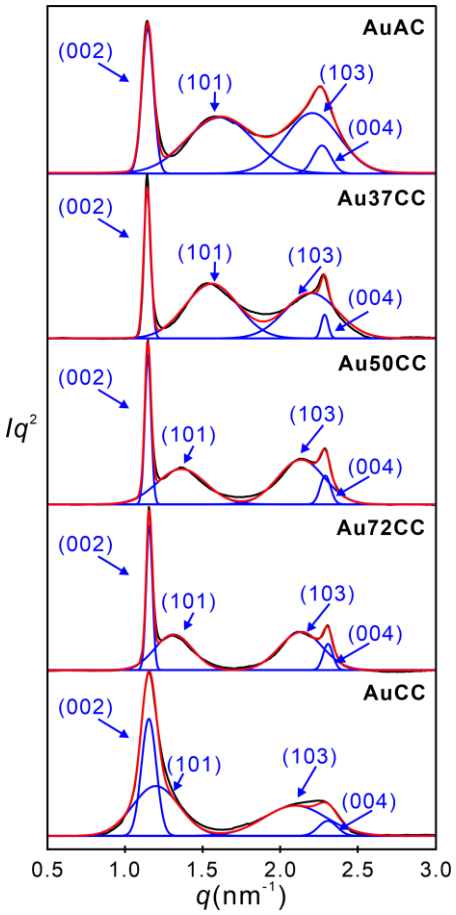

Figure 2. Transmission SAXS curves of unoriented **LC-AuNP** compounds with different **AC**/**CC** ligand ratios. **CC** fraction and the overall graft density are increasing from top to bottom. Experimental = black, resolved components = blue, sum of components = red.

As **CC** fraction and the overall ligand content increase, the broad (101) and (103) move to lower *q* while the sharp (002) and (004) peaks stay fixed. Thus *a*, the width of the unit cell, increases, as shown by the linear plot in Figure 3a; meanwhile the same figure also shows the constant layer spacing (*c*/2). The lateral expansion of the unit cell can be attributed directly to the increase in the organic volume V_{org} (see Table S2). The increase in cell volume between **AuAC** and **AuCC** is

74% (Table 1), which matches exactly the increase in the total volume V_{all} of a LC-coated nanoparticle calculated from TGA, assuming the usual organic density of 0.9 g·cm^{-3}. This close match is further support of the BCT structure.

Table 1. Phase sequence and the lattice parameters of **LC-AuNP**s

Com.	Phase sequence[a]	*a*/ nm[b]	*c*/ nm[b]	V_{cal}/ nm^3[c]
AuAC	BCT 91 Iso	4.17	10.97	191
Au37CC	BCT 78 Iso	4.33	10.99	206
Au50CC	BCT 66 Iso	5.08	10.94	282
Au72CC	BCT 65 Iso	5.33	10.86	309
AuCC	BCT 65 Iso	5.97	10.88	388

[a] Determined by temperature-dependent SAXS, [b] determined by SAXS, [c] unit cell volume. BCT = body-centered tetragonal, Iso = isotropic.

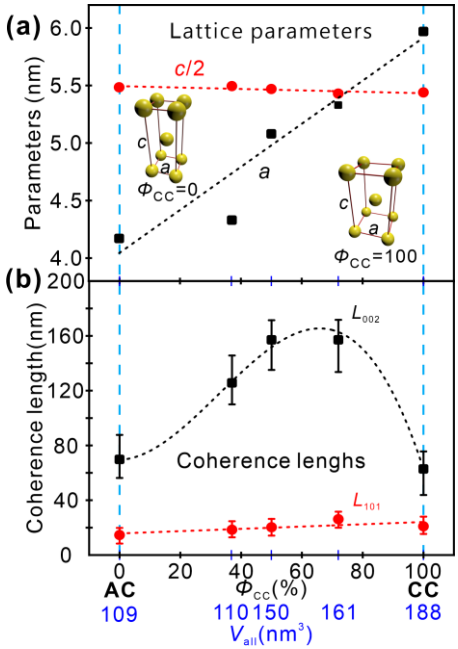

Figure 3. (a) Composition-dependence of unit cell width a and half-height *c*/2. Insets show schematically the lateral expansion of the unit cell (aspect ratio to scale). (b) Composition-dependence of coherence length along [001] and [101] directions.

Volume calculation (Tables 1 and S2) shows that there are two NPs in a unit cell. Since the SAXS pattern is dominated by the gold8, 10, 12, it gives no direct information on the arrangement of the organic corona. Our model of the organization of the organic part is based on the following facts and reasoning. The length of the fully extended ligands is 4.7 nm for **AC** and 4.3 nm for **CC**, and the diameter of an AuNP is ~2 nm, the lattice parameter *c* ~ 11 nm matches the calculated value of ~ 2×4.5+2. Hence, we propose that the mesogens pack head-to-head along *c* axis. Preferred alignment of mesogens is confirmed by POM micrographs recorded with a λ-plate which show that the slow (i.e. mesogen) axis is perpendicular to the layers (Figure6b,g). Considering the tendency for phase separation between rigid and

flexible moieties, we propose that the mesogens pack in continuous modulated egg-box shape layers approximated by the sin*x*×sin*y* surface shown in Figure 4.

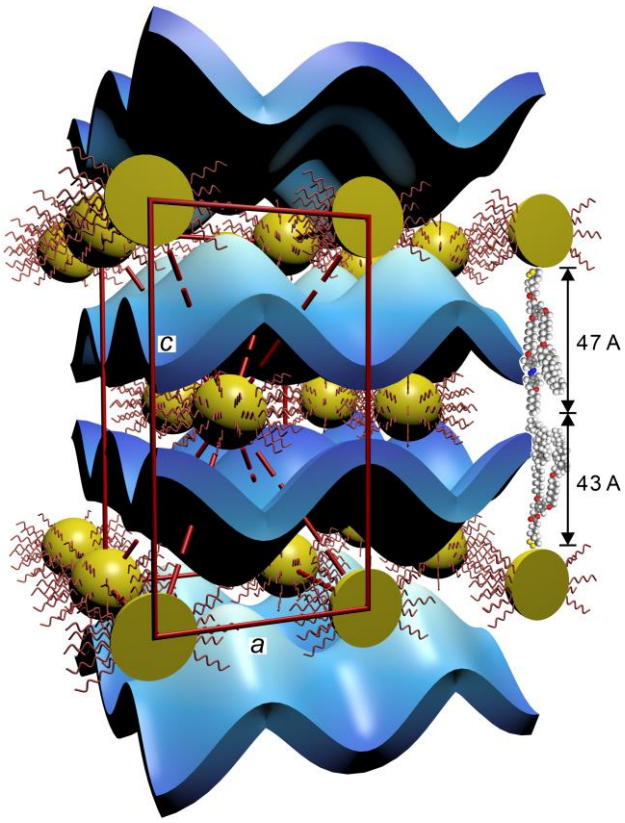

Figure 4. Model of the "egg-box" BCT structure. The blue sinx×siny surface outlines the middle of the layers modulated both along *x* and *y* axes, containing the mesogens. AuNP = yellow, co-ligands = red. One ligand attached to each of the particles on extreme right is shown. The average length of the ligand is 45 Å.

Compared to layer reflections (00*l*), the (*h*0*l*) diffraction peaks are significantly broader (Figure 2), and the associated coherence length ("crystal size", L_{101}) is significantly shorter than L_{002}, the coherence length normal to the layers. L_{101} of ~25 nm corresponds to only ~5 unit cells, remaining nearly constant with composition (Figure 3b). By contrast, stacking of layer is far more regular, the L_{002} varying between 60 and 150 nm (11 to 27 layers). This anisotropy in the degree of order is consistent with mesogens lying along *z*–axis as layer spacing, which is nearly unaffected by composition, is determined by the ligand length. In contrast, *lateral* positional fluctuation has no such restriction, hence positional fluctuations are larger. Interestingly, L_{002} has a maximum at intermediate compositions. A possible reason is the ability of the two ligands to take different preferred positions on the undulated mesogen layer, an option absents in **AuCC** and **AuAC**.

The structure depicted in Figure 4 is unique in LCs. To our knowledge the two-dimensional undulations ("egg-box" type) in the mesogen layer has not been observed previously, although 1D wave undulations,

usually caused by slight taper in molecular shape, are known in some smectics (the Sm-$\tilde{A}$ phase)[30]

Morphologies of thin films of the NPs as observed by TEM are shown in Figure 5a,b. For **AuAC**, the particles are seen to organize in bending rows with inter-row spacing of 5.5 nm. The interparticle distance within the rows is ca 4 nm. The centered rectangular structure that can be seen in the inset is the 2D version of the 3D BCT structure, its projection along [100] direction. The layer spacing of 5.5 nm is equivalent to *c*/2 of the BCT. Micrographs of monolayers of mixed-ligand NPs (Figure S10) appear similar to that of **AuAC**, all with the inter-row spacing of 5.5 nm. By contrast, **AuCC** formed a well-ordered hexagonal monolayer with lattice parameter 6.35 nm, as measured from the Fourier transform (Figure 5b). The hexagonal lattice parameter *a*=6.35 nm means that the layer spacing d_{100} is also 5.5 nm. The lateral expansion of the 2D lattice between **AuAC** and **AuCC**, from rectangular to hexagonal, also mirrors that in the 3D phase.

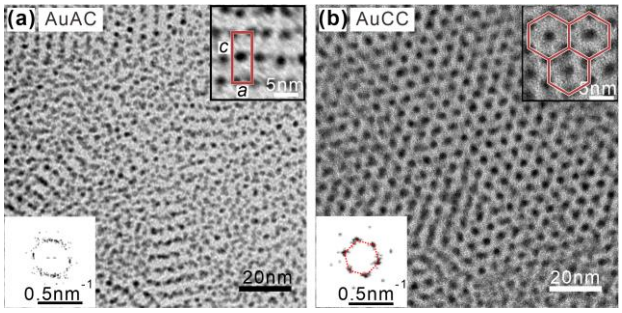

Figure 5. TEM micrographs of nanoparticles (a) **AuAC** and (b) **AuCC**. The insets at top right show an enlarged region, and those at bottom left are the Fourier transforms.

The above BCT structural model is consistent with the POM texture. The λ-plate images in Figure 6b,g show that the slow axis, i.e. the mesogen long axis, is oriented radially in the nearly circular section of the Dupin cyclide marked by the Maltese cross in Figure 6a,f**.** Since these defects consist of concentric circular layers (Figure 6k), the mesogens are perpendicular to the layers, on average. Interestingly, when the polarizer is remover and these defects are viewed through the analyzer only, a dark streak perpendicular to the analyzer is observed in all **LC-AuNP** samples except **AuCC**. As the analyser is rotated, the dark streak rotates with it. Azimuthal scans of transmitted light intensity around the circles in Figure 6d,i for **AuAC** and **AuCC** are shown in Figure 6n. The dark streak and the scans indicate linear dichroism, i.e. anisotropy in plasmonic absorption of the AuNPs, spectrally broad but centred around 550 nm[31] (Figure S11). In contrast, for **AuCC** plasmonic absorption is isotropic, as seen by the uniform reddish colour in Figure 6h-j, independent of analyzer orientation. We attribute the plasmonic dichroism to the interparticle gap within the *xy*-plane (1.9 nm) being only half that of the nearest out-of-plane gap (3.9 nm) for **AuAC** – see Figure 6m23. In contrast, the corresponding gaps for **AuCC** are 3.6 nm and 4.5 nm, both too wide for any near-field

effects and thus too wide to cause dichroism.

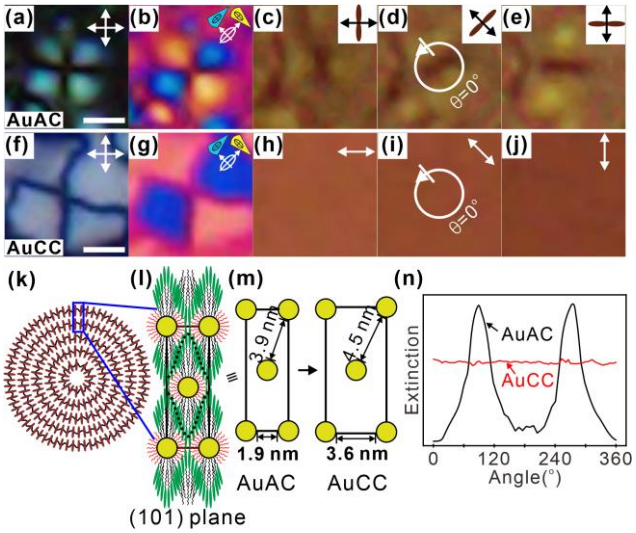

Figure 6. Optical micrographs of a detail of BCT texture of (a-e) **AuAC** and (f-j) **AuCC** (bar =20 μm). (a,f) crossed polarizers, (b,g) with added λ-plate, (c-e) and (h-g) with analyzer only, oriented (c,h) horizontally, (d,i) at 45˚, and (e,j) vertically. The circles in (d) and (i), centered at the centre of a "spherulite" (Dupin cyclide) represent the tracks of the azimuthal scans of transmitted light intensity, Insets in (c-e) show the orientation of the analyzer (double arrow) and of the dark band (double ellipse). The yellow tinge is due to blue-violet absorption by azobenzene. (k) Schematic of the texture detail in (a,b,f,g) showing smectic-like layers of the BCT phase as undulated concentric rings; a detail of (101) plane is shown in (l) (height/width ratio is to scale).(m) Interparticle gap in (101) plane along xy-plane and out of plane for **AuAC** and **AuCC**. (n) Azimuthal scan around circles such as in (d,i). Scans around 6 different circles were averaged.

Limited global orientation can be achieved by shearing (Figures 1b and 7a,b). Both the SAXS and POM with λ-plate in these figures indicate weak preferred alignment of the mesogens along the shear. Consistent with the above plasmonic anisotropy are the visible absorption spectra. Extinction recorded with the polarizer normal to the shear (Figure 7c) is seen to be enhanced in the plasmonic range (>500 nm), while the azobenzene absorption around 400 nm is enhanced when the polarizer is parallel (note that the transition dipole for **A** is ca 30° to the molecular axis[32]).

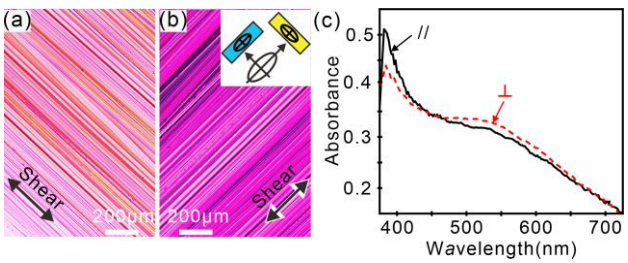

Figure 7. (a,b) Optical micrographs of **AuAC** sheared on a glass slide. Crossed polarizers with added λ-plate. Shear direction is indicated by

double arrow. (c) Polarized UV-vis spectra of **AuAC** sheared parallel (//) and perpendicular (⊥) to the polarizer.

To test the effect of photoisomerization of azobenzene on the state of order of the AuNPs, a powder sample of **AuAC** was irradiated *in-situ* by 365 nm UV light for 120 s while simultaneously recording SAXS patterns in a synchrotron X-ray beam. Photoisomerization of **A** led to the collapse of the tetragonal structure, i.e. isotropization, leaving only short range positional order (Figure 8a). The BCT structure was recovered by irradiation with visible light. The photoisomerization can be repeated numerous times. Reversibility of the switching can be monitored POM as the sample is irradiated *in situ* alternativelt by UV and visible light. Periodic disappearance and appearance of birefringent texture was monitored by following the brightness of the POM field of view. The first 20 cycles are shown in Fig. 8b. As seen, after a small initial drop, the amplitude soon stabilizes. Weak circular dichroism is observed in **A**-containing systems, the azobenzene π-π* CD band at 380 nm only appearing in the BCT phase (Figure S12). This we attribute tentatively to the formation of local chiral clusters, with the 3D BCT lattice resisting global twist.

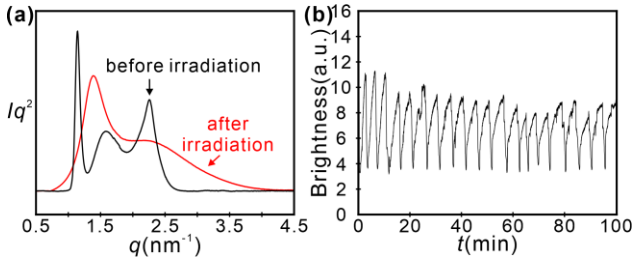

Figure 8. (a) SAXS traces of **AuAC** at room temperature before and after 365 nm UV irradiation for 2 minutes. (b) Mean brightness of POM images of **AuAC** upon alternating UV and visible-light irradiation during the first 21 cycles.

Conclusions

In summary, we synthesized AuNPs grafted with either twin **CC** ligands, Janus-type **AC** ligands, or a mixture of the two. All five synthesized NP types form a body-centred tetragonal superlattice containing unusual alternating 2D modulated “egg-sell” smectic-like mesogen layers. While the interlayer spacing remains constant, the cell width, and with it the closest in-plane interparticle gap, decreases linearly from 5.97 to 4.17 nm with decreasing ligand graft content. This close gold particle approach triggers their near-field in-plane interaction, causing linear plasmonic dichroism, absent in densely grafted nanoparticles. It is shown furthermore that the complex assembly can be reversibly melted and re-formed through azobenzene photoisomerization by repeatedly switching UV-irradiation on and off.

Acknowledgements

This work was supported by National Natural Science Foundation of China (21774099), Science and Technology Agency of Shaanxi

Province (2016KW-050, 2018KWZ-03) and 111 Project 2.0 (BP2018008). We acknowledge beamlines BL16B1 at Shanghai Synchrotron Radiation Facility and B23 at Diamond Light Source for beamtime and experimental support. Part of the characterization was performed at Instrument Analysis Center of Xi'an Jiaotong University.

Conflicts of interest
There are no conflicts to declare.

Keywords: gold • nanoparticles • liquid crystal • plasmonic resonance• photoisomerization

Data availability
The raw SAXS and GISAXS patterns (.tif files) generated in this study are available for download at the figshare database, https://doi.org/10.6084/m9.figshare.18741089

References

[1] Z. J. Wong, Y. Wang, K. O'Brien, J. Rho, X. Yin, S. Zhang, N. Fang, T.-J. Yen and X. Zhang, *J. Opt.*, **2017**, *19*, 084007.
[2] N. Sarfraz and I. Khan, *Chem.-Asian J.*, **2021**, *16*, 1-24.
[3] J.-S. Lee, Y.-M. Kim, J.-H. Kwon, H. Shin, B.-H. Sohn and J. Lee, *Adv. Mater.*, **2009**, *21*, 178-183.
[4] R. A. Alvarez-Puebla, A. Agarwal, P. Manna, B. P. Khanal, P. Aldeanueva-Potel, E. Carbo-Argibay, N. Pazos-Perez, L. Vigderman, E. R. Zubarev, N. A. Kotov and L. M. Liz-Marzan, *Proc. Natl. Acad. Sci. USA*, **2011**, *108*, 8157-8161.
[5] Y. Kim, J. G. Smith and P. K. Jain, *Nat. Chem.*, **2018**, *10*, 763-769.
[6] L. L. Zhu, M. M. Gao, C. K. N. Peh and G. W. Ho, *Mater. Horiz.*, **2018**, *5*, 323-343.
[7] D. Schurig, J. J. Mock, B. J. Justice, S. A. Cummer, J. B. Pendry, A. F. Starr and D. R. Smith, *Science*, **2006**, *314*, 977-980.
[8] X. Mang, X. Zeng, B. Tang, F. Liu, G. Ungar, R. Zhang, L. Cseh and G. H. Mehl, *J. Mater. Chem.*, **2012**, *22*, 11101-11106.
[9] B. Donnio, P. García-Vázquez, J. L. Gallani, D. Guillon and E. Terazzi, *Adv. Mater.*, **2007**, *19*, 3534-3539.
[10] L. Cseh, X. B. Mang, X. B. Zeng, F. Liu, G. H. Mehl, G. Ungar and G. Siligardil, *J. Am. Chem. Soc.*, **2015**, *137*, 12736-12739.
[11] H. Yu, C. Welch, W. Qu, C. J. Schubert, F. Liu, G. Siligardi and G. H. Mehl, *Mater. Horiz.*, **2020**, *7*, 3021-3027.
[12] E. Tomczyk, A. Promiński, M. Bagiński, E. Górecka and M. Wójcik, *Small*, **2019**, *15*, 1902807.
[13] J. M. Wolska, D. Pociecha, J. Mieczkowski and E. Gorecka, *Chem. Commun.*, **2014**, *50*, 7975-7978.
[14] N. Kanayama, O. Tsutsumi, A. Kanazawa and T. Ikeda, *Chem. Commun.*, **2001**, 2640-2641.
[15] M. Draper, I. M. Saez, S. J. Cowling, P. Gai, B. Heinrich, B. Donnio, D. Guillon and J. W. Goodby, *Adv. Funct. Mater.*, **2011**, *21*, 1260-1278.
[16] S. Kumar, S. K. Pal, P. S. Kumar and V. Lakshminarayanan, *Soft Matter*, **2007**, *3*, 896-900.
[17] M. Gupta, S. S. Mohapatra, S. Dhara and S. K. Pal, *J. Mater. Chem. C*, **2018**, *6*, 2303-2310.
[18] H. N. Yu, W. T. Qu, F. Liu and G. H. Mehl, *Chem. Sci.*, **2021**, *12*, 1778-1782.
[19] K. Kanie, M. Matsubara, X. Zeng, F. Liu, G. Ungar, H. Nakamura and A. Muramatsu, *J. Am. Chem. Soc.*, **2012**, *134*, 808-811.
[20] M. Matsubara, W. Stevenson, J. Yabuki, X. Zeng, H. Dong, K. Kojima, S. F. Chichibu, K. Tamada, A. Muramatsu, G. Ungar and K. Kanie, *Chem*, **2017**, *2*, 860-876.
[21] S. A. Bhat, D. S. S. Rao, S. K. Prasad and C. V. Yelamaggad, *Nanoscale Adv.*, **2021**, *3*, 2269-2279.
[22] A. Zep, M. M. Wojcik, W. Lewandowski, K. Sitkowska, A. Prominski, J. Mieczkowski, D. Pociecha and E. Gorecka, *Angew. Chem. Int. Ed.*, **2014**, *53*, 13725-13728.
[23] P. K. Jain and M. A. El-Sayed, *Chem. Phys. Lett.*, **2010**, *487*, 153-164.
[24] X. B. Zeng, F. Liu, A. G. Fowler, G. Ungar, L. Cseh, G. H. Mehl and J. E. Macdonald, *Adv.*

Mater., **2009**, *21*, 1746-1750.
[25] J. Dintinger, B.-J. Tang, X. Zeng, F. Liu, T. Kienzler, G. H. Mehl, G. Ungar, C. Rockstuhl and T. Scharf, *Adv. Mater.*, **2013**, *25*, 1999-2004.
[26] M. Brust, M. Walker, D. Bethell, D. J. Schiffrin and R. Whyman, *J. Chem. Soc., Chem. Commun.*, **1994**, 801-802.
[27] W. Lewandowski, K. Jatczak, D. Pociecha, J. Mieczkowski, *Langmuir* **2013**, *29*, 3404-3410.
[28] M. J. Hostetler, J. E. Wingate, C.-J. Zhong, J. E. Harris, R. W. Vachet, M. R. Clark, J. D. Londono, S. J. Green, J. J. Stokes, G. D. Wignall, G. L. Glish, M. D. Porter, N. D. Evans, R. W. Murray, *Langmuir* **1998**, *14*, 17-30.
[29] W. Lewandowski, T. Łojewska, P. Szustakiewicz, J. Mieczkowski and D. Pociecha, *Nanoscale*, **2016**, *8*, 2656-2663.
[30] P. Oswald, P. Pieranski, Smectic and Columnar Liquid Crystals, CRC Press, Boca Raton **2006**.
[31] P. K. Jain, K. S. Lee, I. H. El-Sayed and M. A. El-Sayed, *J. Phys. Chem. B*, **2006**, *110*, 7238-7248.
[32] P. Uznanski, M. Kryszewski and E. W. Thulstrup, *Spectrochim. Acta A*, **1990**, *46*, 23-27.

Table of Contents Entry

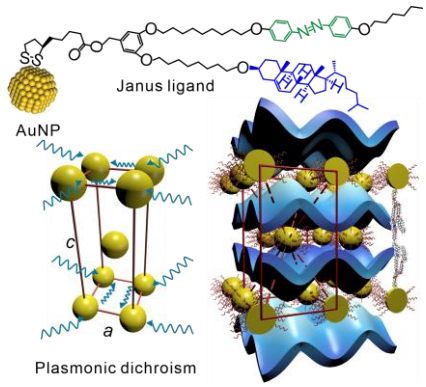

Gold nanoparticles (NP) grafted with mixed-mesogen forked ligands self-assemble in a photoresponsive 3D superlattice with adjustable anisotropic plasmonic absorption. The gold NPs are arranged on a body-centered tetragonal lattice intercalated by doubly-modulated mesogens layers. Reducing graft density reduces the in-layer NP distance enabling near-field plasmonic enhancement. The attached azobenzene mesogen allows repeated photoinduced order-disorder switching.